Journal of Materials Chemistry A

ROYAL SOCIETY OF CHEMISTRY

PAPER

View Article Online
View Journal





Cite this: DOI: 10.1039/d2ta01536f

# A dual-confined lithium nucleation and growth design enables dendrite-free lithium metal batteries†

Lun Li,‡[ab] Huaqiang Fu,‡[a] Jinlong Yang,*[b] Pengyan Wang,[a] Huazhang Zhang,[c] Xin Zhao,[c] Zhitong Xiao,[a] Zhenhui Liu,[d] Zongkui Kou,[a] Zhenbo Wang[b] and Daping He*[ce]

Suppressing lithium (Li) dendrite growth is expected to enable the construction of a reliable Li metal anode for high energy density batteries. However, it is still a huge challenge to synchronize uniform nucleation and controllable growth for complete suppression of Li dendrite formation, because independent confinement of nucleation or growth is hampering the rational design of current Li anodes. Herein, we demonstrate that by anchoring silver (Ag) nanocrystals on the superlithiophilic nitrogen (N) doping site in reduced graphene oxide (Ag/N-rGO) supports, a dual-confined Li nucleation and growth is synchronously realised for producing a stable Li metal anode. Our dual-confined design gives abundant Ag/N interface sites which direct the uniformity of Li nucleation, and provides evenly sized Ag nanocrystals adjacent to N sites which further impose a complete restriction on the disordered Li growth, as rationalized by a combined study comprising experimental observation and theoretical simulations. As a result, our dual-confined Li anode shows a dendrite-free microstructure even after high-capacity and repeated Li plating/stripping. It shows highly stable coulombic efficiency over 99.1% and ultra-long cycle life over 1200 h upon cycling at 2 mA $cm^{-2}$. An LFP//Li@Ag/N-rGO full cell manifests a superior rate capability and a high cycling stability (110.8 mA h $g^{-1}$ at 1C) over 500 cycles.

Received 25th February 2022
Accepted 20th April 2022

DOI: 10.1039/d2ta01536f

rsc.li/materials-a

## Introduction

Lithium (Li) metal serves as the most attractive anode candidate for future Li-based batteries with high energy density due to its highest theoretical capacity (3860 mA h $g^{-1}$), lowest electrochemical potential (−3.04 V *vs.* the standard hydrogen electrode), and low density (0.534 g $cm^{-3}$).[1–3] Nevertheless, the appearance of undesired Li dendrites and severe volume expansion have become two main safety obstacles especially when applying high current density/plating capacity or a continual cycling process. Numerous efforts have been dedicated to relieving these issues, including electrolyte composition optimization,[4–6] stable artificial solid electrolyte interphase (SEI) fabrication,[7–9] and three-dimensional (3D) host utilization.[10,11] Among them, 3D structured frameworks, such as the reduced graphene oxide (rGO) substrate with high specific surface area and better toughness,[12–14] can effectively dissipate the local current density,[15,16] and maintain a stable volume upon cycling.[17,18] However, complete suppression of Li dendrites remains a challenge.

The Li deposition process involves initial nucleation and subsequent growth.[19–21] In general, homogeneous nucleation is highly desired for uniform Li deposition, which is easily achieved by some lithiophilic sites including polar functional groups, *etc.*[22–24] Lithiophilic species with high $Li^+$ affinity can reduce the overpotential during Li nucleation, while producing monodisperse $Li^+$ for directing the homogeneous Li nucleation.[25,26] Lithiophilic heteroatoms (N, O, F, and S) have been established as the most efficient nucleation sites due to their atomic distribution.[27–30] Independent optimization for uniform Li nucleation is not enough to induce a perfectly smooth Li layer unless controllable Li growth must be synchronously realized. Those metals (Ag, Au, and Zn nanoseeds) featuring high solubility in Li have shown a positive effect on guiding uniform Li

[a]School of Materials Science and Engineering, Wuhan University of Technology, Wuhan 430070, China

[b]Guangdong Research Center for Interfacial Engineering of Functional Materials, College of Materials Science and Engineering, Shenzhen University, Shenzhen 518060, China. E-mail: yangjl18@szu.edu.cn

[c]Hubei Engineering Research Center of RF-Microwave Technology and Application, Wuhan University of Technology, Wuhan 430070, China. E-mail: hedaping@whut.edu.cn

[d]College of Material Science and Engineering, Nanjing University of Aeronautics and Astronautics, Nanjing 210016, P. R. China

[e]State Key Laboratory of Silicate Materials for Architectures, Wuhan University of Technology, Wuhan, 430070, P. R. China

† Electronic supplementary information (ESI) available: Experimental details, materials characterization, electrochemical measurements and computational details, and supplementary data, including Videos S1–S6. See https://doi.org/10.1039/d2ta01536f

‡ These authors contributed equally to this work.

growth for constructing a stable Li metal anode.[31–33] The formation of $Li_xM_y$ alloys can increase the affinity with Li and synchronously provide a high strength interface for Li deposition.[11,29,34] Therefore, anchoring the metals around the N doping sites in the integrating electrode materials is highly anticipated for a complete restriction on disordered dendrite growth by dual confining Li nucleation and growth although it is highly challenging.

Herein, we anchor Ag nanocrystals (Ag NCs) on those lithiophilic N-doping sites on the rGO framework and successfully realize a dual-confined Li nucleation and growth. The integrated structure with uniformly distributed N atoms and Ag NCs can synergistically enhance the lithiophilicity, thus regulating the uniform Li nucleation at the interface of Ag/N. Ag NCs successively induce an Li–Ag alloying reaction and direct Li epitaxial growth from the existing nucleus. Under such a dual-confined strategy, a smooth and dense Li deposition can be achieved. The anchored Ag NCs and N sites on the rGO (Ag/N-rGO) electrode manifest stable Li plating/stripping with an ultralow nucleation overpotential (6.8 mV) and a high CE (99.1%). Besides, Li@Ag/N-rGO symmetric cells exhibit a superior rate capability and an ultra-stable cycle life over 1200 h. Moreover, the $LiFePO_4$ (LFP)//Li@Ag/N-rGO full cells also deliver a significantly enhanced rate performance and cycling stability over 500 cycles.

## Results and discussion

### Dual-confined effect of N sites and Ag NCs

Different Li nucleation and growth behaviors on three substrates are depicted in Fig. 1. For the bare Cu substrate, a rough surface with many protrusions has been observed (Fig. S1a and b†). According to the theory of Li dendrite growth,[35] protrusions with high curvature tend to generate a higher electric field which can cause the accumulation of more $Li^+$ and enable $Li^+$ diffusion along all directions, resulting in fluffy Li dendrites. Thus, Li-ions are apt to nucleate with irregular shapes and grow as dendrites (Fig. 1a). Although the surface of the unmodified rGO skeleton is relatively smoother than that of Cu (Fig. S1c and d†), its poor lithiophilicity is also responsible for dendrite formation and low utilization of space between layers (Fig. 1b).[30,36,37] In contrast, the co-existence of N and Ag can highly enhance the lithiophilicity and homogenize Li nucleation. In addition, the $Li_xAg_y$ solid solution layer can further regulate Li growth. This dual-confined Li nucleation and growth design in rGO layers finally yields a smooth and dense Li deposition (Fig. 1c).

### Fabrication and characterization of the Ag/N-rGO substrate

The fabrication of the free-standing Ag/N-rGO substrate is schematically depicted (Fig. S2a†). Firstly, GO solution was well mixed with a certain amount of $AgNO_3$. Then the precursor slurry was blade-coated with a scraper onto a polyethylene terephthalate (PET) board to form a film after drying (Fig. S2b†). Finally, the mixed precursor film was heated and reduced at 600 °C in an argon atmosphere to obtain a 10 meter level of Ag/N-rGO substrate. The unique and stable rGO skeleton endows this composite film with a superior flexibility (Fig. S2c–h†). Thus, the Ag/N-rGO film can sustain various mechanical deformations like bending, rolling, and even repetitive folding.

X-ray diffraction (XRD) patterns of the rGO and Ag/N-rGO substrates are presented in Fig. S3a.† The two peaks at 26.0° and 53.0° correspond to the (002) and (004) planes of the graphitic structure. Besides the rGO composition, Ag/N-rGO also displays three diffraction peaks at 38.0°, 44.2°, and 64.4°, which are ascribed to the planes of metallic Ag (111), (200) and (220) phases (PDF No. 87-0597). In addition, the $I_D/I_G$ value (~1.29) for Ag/N-rGO is larger than that for the rGO (~1.18) substrate, indicating a more defect-accompanied graphene structure of Ag/N-rGO (Fig. S3b†). X-ray photoelectron spectroscopy (XPS) was used to determine the elemental composition and valence state of Ag/N-rGO (Fig. S4a†). The Ag 3d spectrum presents two main peaks at 374.5 and 368.5 eV, which are assigned to $3d_{3/2}$ and $3d_{5/2}$ of zero valence metallic Ag (Fig. 2a).[8,34,38] As depicted in Fig. 2b, the three peaks located at

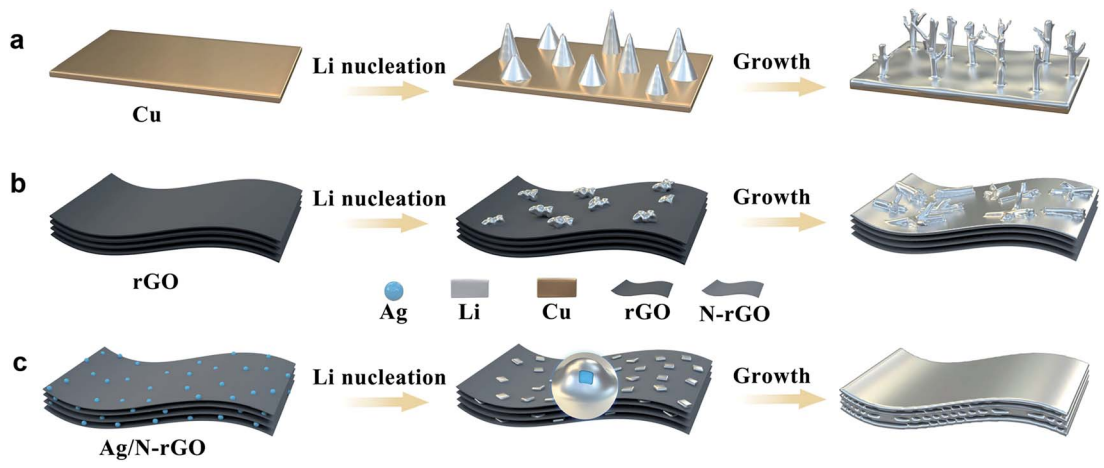


Fig. 1 Schematic depicting of Li nucleation and growth behaviors on three substrates. Deposition of Li on (a) Cu, (b) rGO, and (c) Ag/N-rGO substrates.

 

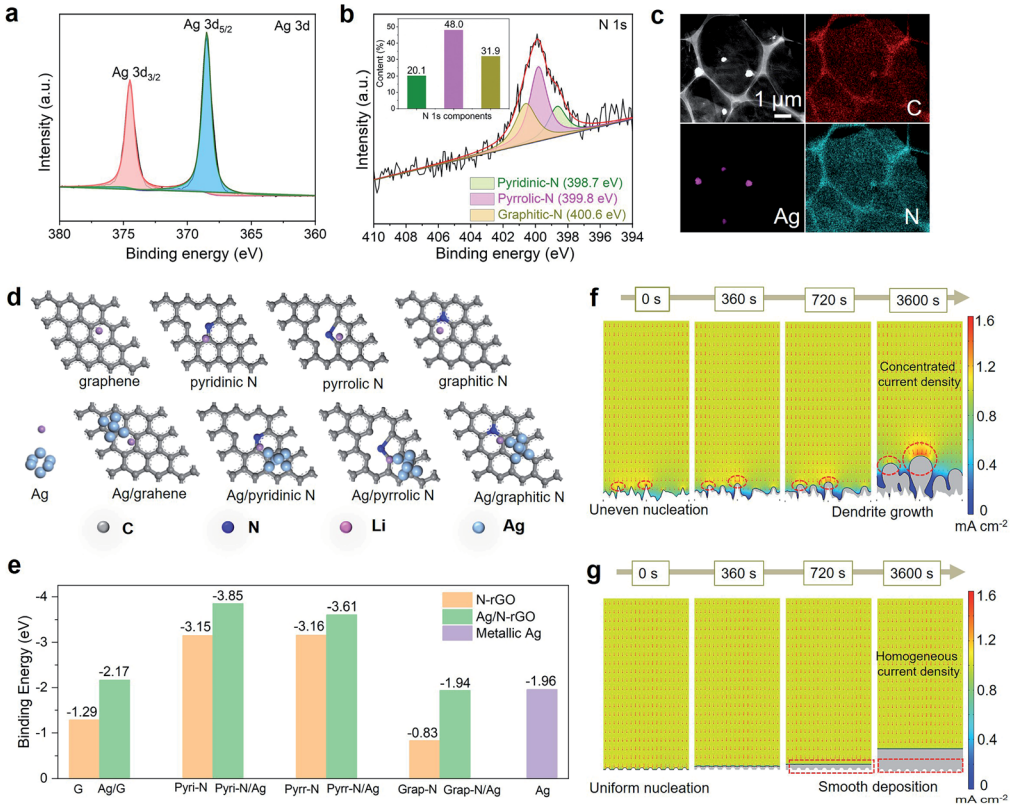


Fig. 2 Dual-confined Li anode design. XPS spectra of (a) Ag 3d and (b) N 1s of Ag/N-rGO. (c) Elemental mapping of C, Ag, and N elements in Ag/N-rGO sheets. (d) Structure modeling of a Li atom deposited on various substrates. (e) Calculated binding energy of a Li atom with different substrates. (f and g) COMSOL simulation of current density distributions and Li deposition morphology evolution on substrates with (f) randomly distributed nucleation and (g) Ag/N-rGO substrate with uniformly distributed nucleation around Ag NCs.

398.7, 399.8, and 400.6 eV confirm the existence of pyridinic N, pyrrolic N and graphitic N, respectively.[25,39,40] The peaks of C–N and C=C in the C 1s spectrum (Fig. S4b†) further confirm the N-doped graphene structure. According to the XPS results (Table S1†), the total content of N atoms is determined to be 5.8%. Lithiophilic N sites including pyridinic N and pyrrolic N together account for 68.1% of the total N atoms (Fig. 2b inset). This result favors the affinity of $Li^+$ with N-rGO, thus promoting uniform nucleation.

In addition, from the scanning electron microscope (SEM) image, it is observed that Ag NCs with a diameter of ~400 nm are evenly dispersed on the N-rGO surface (Fig. S5a†). According to thermogravimetric results, the weight ratio of Ag NCs is determined to be ~18.0% in the Ag/N-rGO composite (Fig. S6†). The cross-sectional SEM image in Fig. S5b and c† clearly demonstrate the orderly stacked layer structure with a thickness of ~40 μm. Although the Ag/N-rGO film is thicker than the bare Cu foil (~8.0 μm), its specific area mass (1.1 mg $cm^{-2}$) is significantly lower than that of Cu foil (7.2 mg $cm^{-2}$) (Fig. S7†), which is beneficial for the construction of high gravimetric energy density Li metal batteries. The high-resolution transmission electron microscopy (HRTEM) image of Ag/N-rGO shows a lattice spacing of 0.24 nm (Fig. S5d†), which is in accord with the (111) plane of metallic Ag. Meanwhile, elemental mapping was recorded to illustrate the uniform element distribution for C, Ag, and N (Fig. 2c). Notably, the Ag NCs are still anchored on the N-rGO layers after heavy ultrasonication, confirming a strong adhesion of Ag NCs with N-rGO sheets.

## Validation of dual-confined design of Li nucleation and growth

Density functional theory (DFT) calculations were introduced to evaluate Li nucleation on different substrates (Fig. 2d). The binding energies (BEs) based on DFT calculations are summarized in Fig. 2e. The low BE (−1.29 eV) of graphene with a Li atom indicates a weak interaction between them. When N atoms were doped, the pyridinic N and pyrrolic N doped graphene exhibit higher BEs of −3.15 and −3.16 eV. These BEs are also higher than that of graphitic N (−0.83 eV), suggesting that pyridinic N and pyrrolic N are the main lithiophilic N species, which is consistent with other reported studies.[18] Because Ag can participate in the bonding of Li, the BE between the Li atom and Ag NCs (−1.96 eV) is also higher than that between the Li atom and graphene (−1.29 eV). As a result, the BE of this composite is increased to −2.17 eV after introducing Ag NCs into the graphene. These results reveal that the pyridinic N, pyrrolic N, and Ag NCs exhibit stronger binding with Li atoms than the graphene framework. Therefore, the synergistic effects of N sites and Ag NCs were also studied. Significantly improved

BEs of −3.85 for Li–Ag/pyridinic N-rGO and −3.61 for Li–Ag/pyrrolic N-rGO are acquired. These results demonstrate that when coupled with Ag NCs, the N-rGO demonstrates reinforced lithiophilic properties and a reduced energy barrier for nucleation, thus aiding uniform Li nucleation. Optimized composite models show that Ag NCs eventually settle on the hexatomic carbon ring which is connected to N atoms (Fig. S8†). Meanwhile, the Li atom is located between Ag NCs and the N-doped carbon ring, indicating that initial Li nucleation on Ag/N-rGO tends to start from the interface between Ag NCs and pyridinic N and pyrrolic N. Such an interface nucleation gradually spreads to the surface of Ag NCs until fully coating them. Based on all of this, the layered Ag/N-rGO can achieve a uniform Li nucleation that well integrated with the Li layer.

Phase-field simulation using COMSOL Multiphysics was further carried out to model the subsequent evolution of Li growth. At the initial nucleation stage, Li first deposits to form a planar architecture which uniformly covers the individual Ag NCs, and all Li nuclei are evenly distributed compared with agglomerated Li blocks on rGO or disordered Li dendrites on Cu substrates (Fig. S9†). Correspondingly, the Cu and rGO cells are designed as substrates filled with random Li nuclei (Fig. S10a†), where $Li^+$ ions tend to concentrate at the tips without the regulation of Ag NCs (Fig. S11a and Video S1†) which is driven by the locally concentrated current density and electric field (Fig. 2f and Video S2†). Therefore, Li metal prefers to grow along the tip. As the deposition capacity increases, the Li tips grow bulky and more $Li^+$ ions migrate here, aggravating the difference of $Li^+$ concentration gradient between the bottom and the tips. As a result, $Li^+$ at the bottom can't be supplied fast enough to maintain the same deposition rate as at the tip. Finally, the adverse Li deposition is exacerbated, evolving into severe dendrite morphology. Even on an N-rGO substrate, metallic Li still achieves an uneven growth and a rugged surface (Fig. S12 and Videos S3 and S4†). In terms of the uniform nucleation on Ag/N interface sites (Fig. S10b†), a homogeneous $Li^+$ concentration gradient and distribution throughout the electrode is observed (Fig. S11b and Video S5†), which also leads to a uniform current density distribution and electric field (Fig. 2g and Video S6†). Subsequently, Li prefers to deposit around the existing Li nucleus to induce a Li–Ag alloying reaction and therefore a solid solution-based Li–Ag alloy phase (Fig. S13†) which surrounds Ag NCs. With the guidance of the Li–Ag alloy, saturated Li species extend outward. As a consequence, a curvature enhanced coverage is formed until they are epitaxially connected to each other on the substrate. As the plating time increases, a smooth and compact Li deposition morphology is formed without any dendrite. Subsequently, Li deposits on the formed Li plane with a dense deposition and smooth surface.

### Practical deposition morphology of Li metal on three substrates

To investigate the electrodeposition behavior under real conditions, we assembled three asymmetric Li//Cu, Li//rGO and Li//Ag/N-rGO half cells and carried out SEM to reveal the morphology evolution of deposited Li at 1 mA $cm^{-2}$ for area capacities of 1, 2 and 4 mA h $cm^{-2}$. At a high deposition capacity of 4 mA h $cm^{-2}$, the Ag/N-rGO shows an ultralow nucleation overpotential of 6.8 mV which is much smaller than those of rGO (26.1 mV) and Cu (53.7 mV) electrodes (Fig. 3a). The low nucleation overpotential of the Ag/N-rGO electrode undoubtedly decreases the energy barrier for uniform Li nucleation. Specifically, the voltage platform of initial Li nucleation starts from a deposition capacity of around 0.2 mA h $cm^{-2}$. At this stage, Li first deposits to form a planar architecture with distinct wrinkles at the edges, which uniformly covers the individual Ag NCs (Fig. 3a, inset). Such an initial morphology indicates that metallic Li first nucleates with a uniform planar morphology without dendrites.

To further clarify the optimized Li growth morphology based on uniform nucleation, controlled SEM analysis of subsequent deposition behavior was systematically performed. Fig. 3b and c show that with deposition capacities of 1 and 2 mA h $cm^{-2}$ on bare Cu, some agglomerated Li lumps with diameters of 5–10 μm are formed randomly besides a smooth Li metal layer. When the Li plating capacity is increased to 4 mA h $cm^{-2}$, severe vertical growth of Li dendrites occurs outside of the Cu surface (Fig. 3d). Similarly, aggressive Li dendrite clusters can also be discovered on the rGO substrate under various capacities of 1, 2 and 4 mA h $cm^{-2}$ (Fig. 3e–g). These coarse Li dendrites with high tortuosity can be agglomerated and linked by some short dendrites and Li bulk during growth.

Compared with the Cu and rGO substrates, the deposition behavior of Li metal on the Ag/N-rGO substrate is highly improved. From Fig. 3h, it is observed that, when Li metal was deposited on the Ag/N-rGO substrate with a capacity of 1 mA h $cm^{-2}$, many elliptic Li particles with size of ~3 μm are evenly distributed. Upon further increasing the deposition capacity to 2 mA h $cm^{-2}$, the elliptic Li particles are closely connected to form a compact structure (Fig. 3i). As the capacity is increased to 4 mA h $cm^{-2}$, deposited Li forms a more compact and smoother surface without any dendrite (Fig. 3j). Accordingly, Li deposited on Ag/N-rGO shows a minimum thickness of 19.0 μm compared with those on rGO (23.8 μm) and Cu (31.0 μm) (Fig. S14a–c†). Furthermore, the nanogaps of Ag/N-rGO are filled by Li. However, only a few Li particles were observed between the pristine rGO layers. Moreover, the effects of different current densities during deposition (2 and 4 mA $cm^{-2}$) and stripping (1 and 2 mA $cm^{-2}$) on the three substrates are also systematically studied. Clearly, Li@Ag/N-rGO substrates exhibited smoother morphologies after deposition (Fig. S15a–f†) and fewer dead dendrites after stripping (Fig. S15g–l†). This dendrite-free behavior verifies the huge advantages of the lithiophilic Ag/N-rGO substrate for high-capacity and long-term Li plating/stripping. These experimental SEM images are also consistent with the simulation results, demonstrating the validity of dual-confined nucleation and growth in suppressing Li dendrites.

### Electrochemistry of Li metal plating/stripping on the three substrates

To assess the cycling reversibility of the plating/stripping behaviors, the CEs of the Ag/N-rGO substrate under area

 

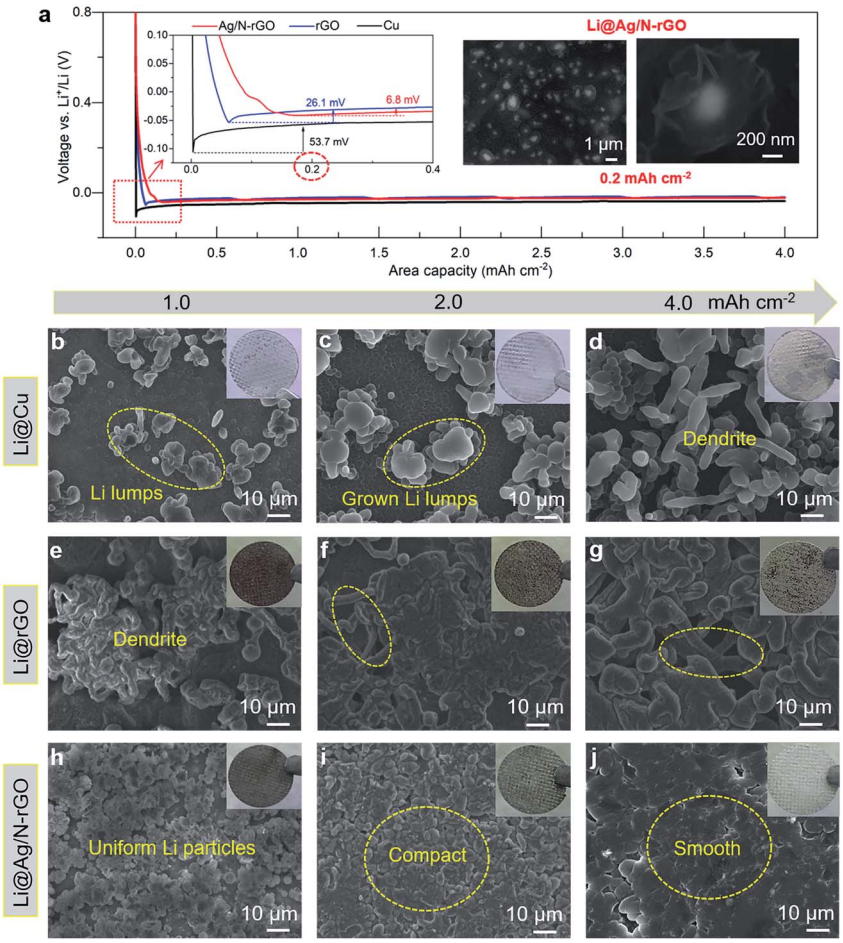


Fig. 3 Deposition behaviors of Li metal on the three substrates. (a) Voltage–capacity profiles of Cu, rGO, and Ag/N-rGO at 1 mA $cm^{-2}$, insets are the enlarged image of nucleation overpotential and SEM images at deposition capacities of 0.2 mA h $cm^{-2}$. (b–j) Top view of (b–d) Cu, (e–g) rGO and (h–j) Ag/N-rGO electrodes after plating at (b, e, and h) 1 mA h $cm^{-2}$, (c, f, and i) 2 mA h $cm^{-2}$, and (d, g, and j) 4 mA h $cm^{-2}$.

capacities of 1 and 2 mA h $cm^{-2}$ at 1 mA $cm^{-2}$ were tested. After several cycles of activation, the Ag/N-rGO manifests a high CE of ~99.1% for more than 160 cycles at 1 mA $cm^{-2}$ for 1 mA h $cm^{-2}$ (Fig. 4a). In contrast, the rGO substrate shows an obvious CE fluctuation during cycling, and the CE of the Cu electrode rapidly drops below 60% only after 80 cycles. For further unveiling the positive effect of Ag/N-rGO compared with pure rGO, their voltage profiles for the first cycle were analyzed (Fig. 4b and S16†). The corresponding voltage gap/overpotential of Ag/N-rGO is 53.2 mV/4.6 mV, which are much smaller than those of the rGO substrate (98.5 mV/20.4 mV). Meanwhile, the voltage profiles of Ag/N-rGO at various cycles are highly overlapped (Fig. 4c), demonstrating a stable Li plating/stripping behavior. Moreover, when the plating capacity is set at 2 mA h $cm^{-2}$, the Li plating/stripping behaviors on the Ag/N-rGO substrate are also stable and consistent. As depicted in Fig. 4d, the CE of Ag/N-rGO can maintain at 98.5% even after 80 cycles, which is highly enhanced compared with rGO and bare Cu electrodes. Furthermore, the Ag/rGO electrode without N sites also showed inferior performance to Ag/N-rGO (Fig. S17†), verifying the critical role of Ag/N sites.

Symmetric cells were also assembled to evaluate long-term cyclability and ion transport capability. All the substrates were electroplated with 3 mA h $cm^{-2}$ to obtain Li@Cu, Li@rGO, and Li@Ag/N-rGO electrodes before symmetric cells were assembled. The overpotentials of Li@Cu and Li@rGO symmetric cells increase sharply after 220 and 280 h, respectively. Comparatively, the Li@Ag/N-rGO symmetric cell shows a reversible and consistent voltage profile over 1200 h at 2 mA $cm^{-2}$ for 1 mA h $cm^{-2}$ (Fig. 4e), showing obvious advantages in cycle life (Table S2†). Moreover, the electrochemical impedance spectroscopy (EIS) analysis further reveals a lower interfacial charge transfer resistance for the Li@Ag/N-rGO (49.7 Ω) electrode compared to the Li@rGO (67.5 Ω) and bare Li@Cu (102.8 Ω) electrodes (Fig. 4f), indicating the improved kinetics of Li deposition by the lithiophilic N and Ag sites on the Ag/N-rGO substrate. Correspondingly, an excellent rate performance was also acquired for the Li@Ag/N-rGO symmetric cell. During the change of current density from 1 to 4 mA $cm^{-2}$, Li@Ag/N-rGO symmetric cells manifest a gradually increased voltage hysteresis from 16.1 to 22 and 30 mV (Fig. 4g). Consequently, the Ag/N-rGO substrate enables a remarkable cycling stability and a faster kinetics during Li plating/stripping.

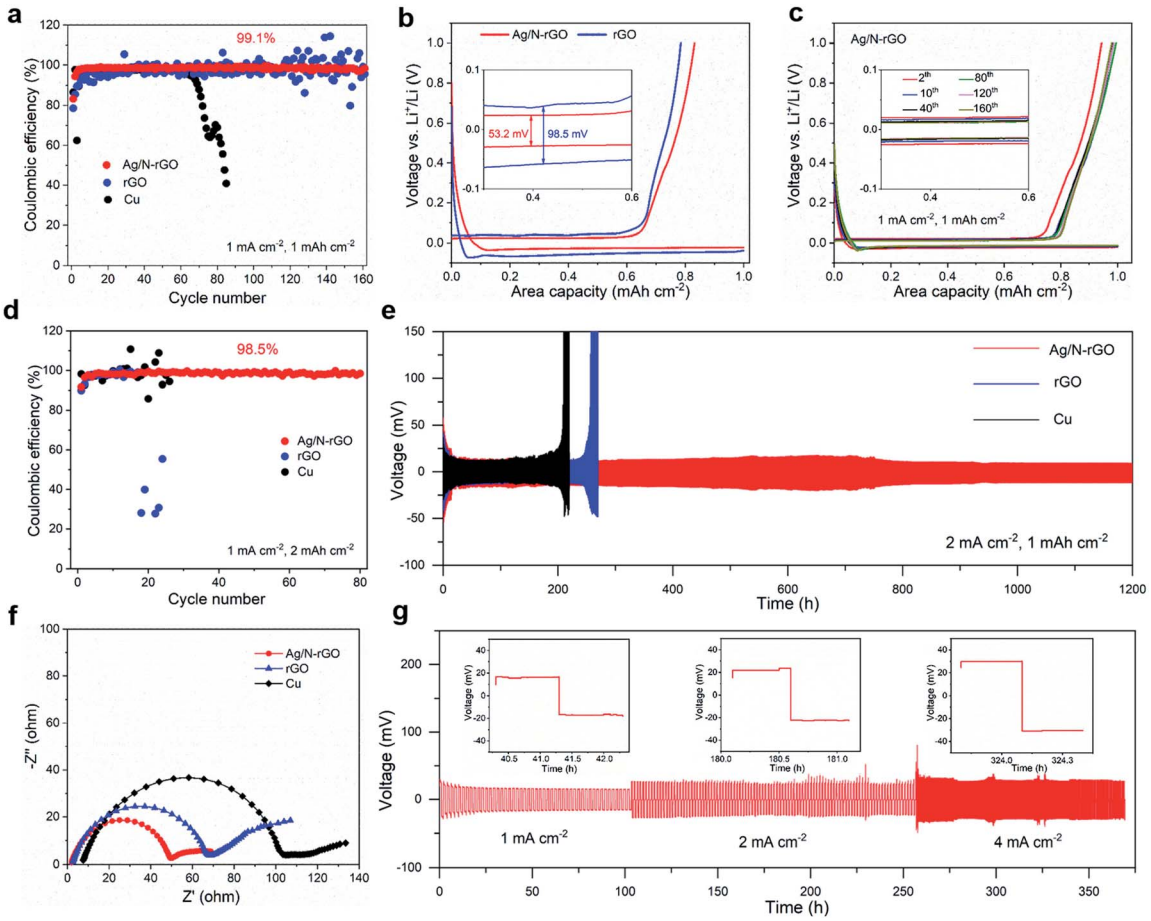


Fig. 4 Electrochemistry of Li metal plating/stripping on the three substrates. (a) CEs of Cu, rGO, and Ag/N-rGO at 1 mA cm$^{-2}$ for an area capacity of 1 mA h cm$^{-2}$. (b) The first plating/stripping curves for rGO and Ag/N-rGO substrates. (c) Li plating/stripping profiles for Ag/N-rGO at different cycles. (d) CEs for Cu, rGO, and Ag/N-rGO with an area capacity of 2 mA h cm$^{-2}$. (e) Cycling stability comparisons of symmetric cells based on Li@Cu, Li@rGO and Li@Ag/N-rGO, respectively. (f) Impedance spectra of Cu, rGO, and Ag/N-rGO electrodes after plating Li with a capacity of 4 mA h cm$^{-2}$. (g) Rate capability of Li@Ag/N-rGO for symmetric cells.

## Li metal morphology on the three substrates after cycling

To further investigate Li plating/stripping features on different substrates after repeated cycling, the Li morphologies after the 80$^{th}$ plating at 1 mA cm$^{-2}$/1 mA h cm$^{-2}$ were recorded. Particularly, most Li layers were easily detached from the Cu substrate during the disassembling process. The remaining part was studied in Fig. 5a and b. The Cu substrate is covered with fluffy Li dendrites mixed with needle-like filaments, which may lead to serious safety problems. Due to loose deposition, the inhomogeneous Li thickness can reach at least 27.3 μm after 80 cycles. As for the rGO substrate, a disordered surface consisting of Li dendrites, dead Li and dispersed Li chunks can still be observed (Fig. 5c). The thickness of Li layers is decreased to 18.2 μm and a porous deposition is still demonstrated (Fig. 5d). After lithiophilic N and Ag NCs are introduced to rGO, Li deposition on the Ag/N-rGO substrate exhibits a smooth and dendrite-free surface (Fig. 5e) accompanied by a more even and compact thickness of 14.5 μm (Fig. 5f). Moreover, the layered structure of Ag/N-rGO is well maintained after cycling, indicating the superiority of Ag/N-rGO in restraining volume expansion.

## Electrochemical properties of the full cells

To confirm the effectiveness of Ag/N-rGO in practical applications, full cells matching Li@Cu, Li@rGO and Li@Ag/N-rGO

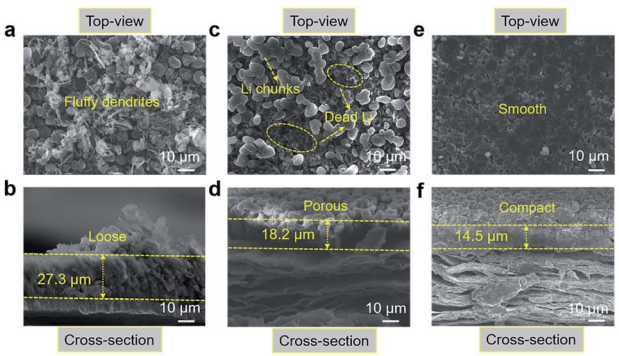


Fig. 5 Li metal morphology on the three substrates after cycling. Top-view and cross-sectional images of Li metal with a capacity of 3 mA h cm$^{-2}$ deposited on (a and b) Cu, (c and d) rGO, and (e and f) Ag/N-rGO substrates after cycling 80 times at 1 mA cm$^{-2}$ for 1 mA h cm$^{-2}$.

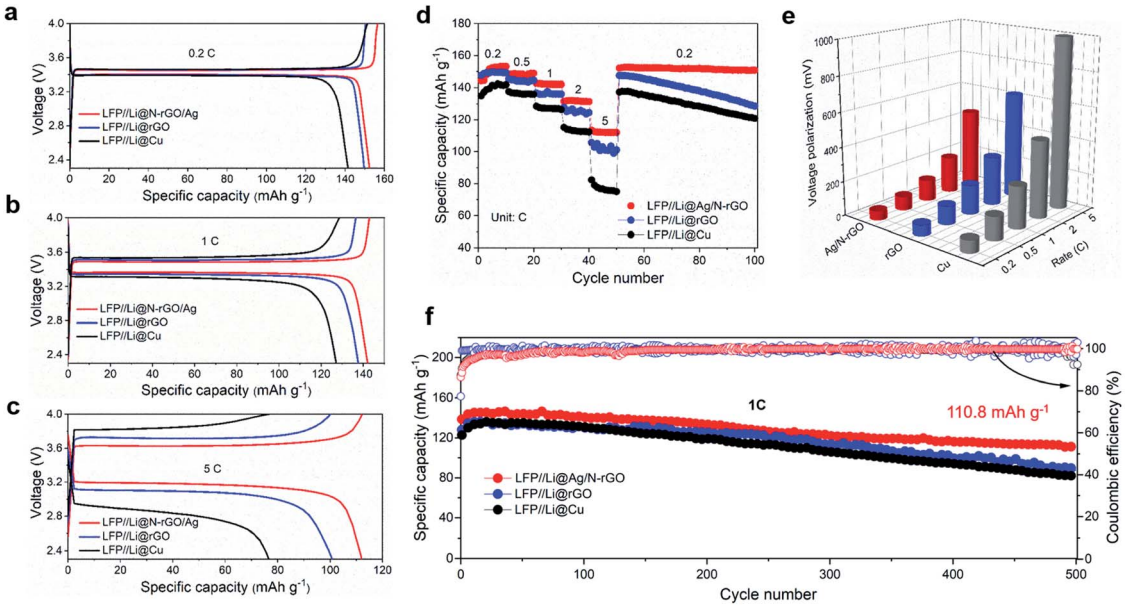


Fig. 6 Electrochemical properties of the full cells. (a–c) Charge–discharge curves of LFP//Li@Cu, LFP//Li@rGO, and LFP//Li@Ag/N-rGO full cells at 0.2, 1, and 5C, respectively. (d) Rate performance and (e) the corresponding voltage polarizations of the three types of full cells. (f) Cycling performance of the three types of full cells at 1C.

anodes with the LFP cathode were assembled, respectively. The typical discharge–charge profiles of LFP with different anodes are compared in Fig. 6a–c. The LFP//Li@Ag/N-rGO full cell delivers higher specific capacity at multiple current densities (0.2–5C, 1C = 170 mA $g^{-1}$) than full cells using Li@rGO and bare Li@Cu anodes, which confirms the positive effect of Ag/N-rGO on boosting the specific capability of the metallic Li anode. Even when tested at 5C, the capacity can still reach up to 112.2 mA h $g^{-1}$, which obviously exceeds those of LFP//Li@rGO (102.2 mA h $g^{-1}$) and LFP//Li@Cu (77.0 mA h $g^{-1}$) full cells (Fig. 6d). Another impressive superiority of the Li@Ag/N-rGO anode is verified by the low voltage polarization. As displayed in Fig. 6e, the full cell of LFP//Li@Ag/N-rGO exhibits a smaller polarization than the other full cells at 0.2C. When the current density increases to 5C, the polarization difference becomes more obvious. Specifically, the polarization voltage reaches up to 997.7 mV for LFP//Li@Cu, 621.6 mV for LFP//Li@rGO, and 457.6 mV for LFP//Li@Ag/N-rGO, which further demonstrates the favorable kinetics of the Li@Ag/N-rGO anode.

Furthermore, the LFP//Li@Ag/N-rGO full cells display an initial capacity of 138.5 mA h $g^{-1}$ at 1C and achieve a capacity retention of 80% (110.8 mA h $g^{-1}$) over 500 cycles. Comparatively, the capacities of LFP//Li@rGO and LFP//Li@Cu heavily decay to 87.5 mA h $g^{-1}$ and 81.8 mA h $g^{-1}$, respectively, which are only 68.4% and 66.2% of their initial capacities (Fig. 6f). Besides, LFP//Li@Ag/N-rGO full cells exhibit a stable and higher CE (99.8%) while an obvious CE fluctuation is observed on the other two full cells using anodes that have not been modified with N and Ag. The SEM images of Li@Cu, Li@rGO and Li@Ag/N-rGO after cycling in full cells are shown in Fig. S18a–c.† Compared with Li@Cu and Li@rGO anodes, Li@Ag/N-rGO still reveals a more ordered and smoother surface. The higher content of LiF in the Li@Ag/N-rGO anode can construct a stable SEI layer to maintain the stability of the Li@Ag/N-rGO anode and prevent the formation of Li dendrites (Fig. S18d–i†). Based on all of this, this LFP//Li@Ag/N-rGO full cell presents an advanced electrochemical performance, confirming the superiority of the Li@Ag/N-rGO anode which is obtained by the dual-confined nucleation and growth strategy.

## Conclusion

In summary, we demonstrate a dual-confined Li anode to completely suppress dendrite growth based on a superlithiophilic Ag/N-rGO substrate. DFT calculations and COMSOL simulations deeply demonstrate the lithiophilic nature and the smooth morphology evolution, verifying the feasibility of this design. Due to the synergistic effect of lithiophilic N and Ag sites, a homogeneous nucleation is realized. Using the alloying effect of Ag NCs, the subsequent Li growth rate is tuned to be uniform. Therefore, a smooth and dense Li deposition morphology is achieved even at a high deposition capacity of 4 mA h $cm^{-2}$. The Li@Ag/N-rGO anode displays enhanced CE (99.1%) and ultra-stable cycle life over 1200 h at 2 mA $cm^{-2}$. Furthermore, the assembled LFP//Li@Ag/N-rGO full cells also display an excellent rate performance and remarkable cycling stability (110.8 mA h $g^{-1}$) over 500 cycles. This work verifies the effectiveness of our design for constructing dual lithiophilic sites, providing a theoretical reference for high-safety and high-energy Li-based batteries.

## Author contributions

The manuscript was written through contributions of all authors. All authors have given approval to the final version of the manuscript. L. L. and D. P. H. conceived the idea and designed the experiments. J. L. Y., Z. B. W., Z. K. K. and D. P. H.

oversaw the project progress. L. L. and H. Q. F. performed the main experiments and analysed the data. P. Y. W. performed detailed computations. H. Z. Z., X. Z., Z. T. X. and Z. H. L. participated in the manuscript revision. L. L., J. L. Y. and D. P. H. wrote the manuscript.

## Conflicts of interest

There are no conflicts to declare.

## Acknowledgements

This work was financially supported by the National Natural Science Foundation of China (52172217), Natural Science Foundation of Guangdong Province (2021A1515010144), and 2018 National Key R&D Program of China (257). The authors also acknowledge the Center for Materials Research and Analysis at the Wuhan University of Technology for TEM and image suggestions from Dr Xiaoqing Liu.

## Notes and references

1 D. Lin, Y. Liu and Y. Cui, *Nat. Nanotechnol.*, 2017, **12**, 194–206.
2 T. T. Zuo, Y. X. Yin, S. H. Wang, P. F. Wang, X. Yang, J. Liu, C. P. Yang and Y. G. Guo, *Nano Lett.*, 2018, **18**, 297–301.
3 C. Niu, H. Pan, W. Xu, J. Xiao, J. G. Zhang, L. Luo, C. Wang, D. Mei, J. Meng, X. Wang, Z. Liu, L. Mai and J. Liu, *Nat. Nanotechnol.*, 2019, **14**, 594–601.
4 A. J. Louli, A. Eldesoky, R. Weber, M. Genovese, M. Coon, J. deGooyer, Z. Deng, R. T. White, J. Lee, T. Rodgers, R. Petibon, S. Hy, S. J. H. Cheng and J. R. Dahn, *Nat. Energy*, 2020, **5**, 693–702.
5 Q. Wang, C. Yang, J. Yang, K. Wu, C. Hu, J. Lu, W. Liu, X. Sun, J. Qiu and H. Zhou, *Adv. Mater.*, 2019, **31**, 1903248.
6 H. Liu, X. Yue, X. Xing, Q. Yan, J. Huang, V. Petrova, H. Zhou and P. Liu, *Energy Storage Mater.*, 2019, **16**, 505–511.
7 Y. Liu, Y. K. Tzeng, D. Lin, A. Pei, H. Lu, N. A. Melosh, Z. X. Shen, S. Chu and Y. Cui, *Joule*, 2018, **2**, 1595–1609.
8 Z. T. Wondimkun, W. A. Tegegne, J. Shi-Kai, C. J. Huang, N. A. Sahalie, M. A. Weret, J. Y. Hsu, P. L. Hsieh, Y. S. Huang, S. H. Wu, W. N. Su and B. J. Hwang, *Energy Storage Mater.*, 2021, **35**, 334–344.
9 P. Zhai, T. Wang, H. Jiang, J. Wan, Y. Wei, L. Wang, W. Liu, Q. Chen, W. Yang, Y. Cui and Y. Gong, *Adv. Mater.*, 2021, **33**, 2006247.
10 S. Zhang, W. Deng, X. Zhou, B. He, J. Liang, F. Zhao, Q. Guo and Z. Liu, *Mater. Today Energy*, 2021, **21**, 100770.
11 H. Wang, P. Hu, X. Liu, Y. Shen, L. Yuan, Z. Li and Y. Huang, *Adv. Sci.*, 2021, **8**, 2100684.
12 Z. Lu, Z. Zhang, X. Chen, Q. Chen, F. Ren, M. Wang, S. Wu, Z. Peng, D. Wang and J. Ye, *Energy Storage Mater.*, 2018, **11**, 47–56.
13 Y. Zhou, Y. Han, H. Zhang, D. Sui, Z. Sun, P. Xiao, X. Wang, Y. Ma and Y. Chen, *Energy Storage Mater.*, 2018, **14**, 222–229.
14 S. Liu, A. Wang, Q. Li, J. Wu, K. Chiou, J. Huang and J. Luo, *Joule*, 2018, **2**, 184–193.
15 W. Deng, W. Zhu, X. Zhou and Z. Liu, *Energy Storage Mater.*, 2018, **15**, 266–273.
16 P. Xue, S. Liu, X. Shi, C. Sun, C. Lai, Y. Zhou, D. Sui, Y. Chen and J. Liang, *Adv. Mater.*, 2018, **30**, 1804165.
17 C. Zhang, S. Liu, G. Li, C. Zhang, X. Liu and J. Luo, *Adv. Mater.*, 2018, **30**, 1801328.
18 D. Lin, Y. Liu, Z. Liang, H. W. Lee, J. Sun, H. Wang, K. Yan, J. Xie and Y. Cui, *Nat. Nanotechnol.*, 2016, **11**, 626–632.
19 X. Chen, X. R. Chen, T. Z. Hou, B. Q. Li, X. B. Cheng, R. Zhang and Q. Zhang, *Sci. Adv.*, 2019, **5**, eaau7728.
20 S. Li, Y. Ma and B. Wei, *Energy Environ. Mater.*, 2021, **4**, 103–110.
21 H. Wu, H. Jia, C. Wang, J.-G. Zhang and W. Xu, *Adv. Energy Mater.*, 2021, **11**, 2003092.
22 S. Ha, D. Kim, H. K. Lim, C. M. Koo, S. J. Kim and Y. S. Yun, *Adv. Funct. Mater.*, 2021, **31**, 2101261.
23 P. Zhai, T. Wang, W. Yang, S. Cui, P. Zhang, A. Nie, Q. Zhang and Y. Gong, *Adv. Energy Mater.*, 2019, **9**, 1804019.
24 S. Li, Z. Luo, H. Tu, H. Zhang, W. Deng, G. Zou, H. Hou and X. Ji, *Energy Storage Mater.*, 2021, **42**, 679–686.
25 T. S. Wang, X. Liu, X. Zhao, P. He, C. W. Nan and L. Z. Fan, *Adv. Funct. Mater.*, 2020, **30**, 2000786.
26 P. Xue, C. Sun, H. Li, J. Liang and C. Lai, *Adv. Sci.*, 2019, **6**, 1900943.
27 S. Liu, A. Wang, Q. Li, J. Wu, K. Chiou, J. Huang and J. Luo, *Joule*, 2018, **2**, 184–193.
28 Z. Xu, L. Xu, Z. Xu, Z. Deng and X. Wang, *Adv. Funct. Mater.*, 2021, **31**, 2102354.
29 Z. Li, X. Li, L. Zhou, Z. Xiao, S. Zhou, X. Zhang, L. Li and L. Zhi, *Nano Energy*, 2018, **49**, 179–185.
30 R. Zhang, X.-R. Chen, X. Chen, X.-B. Cheng, X.-Q. Zhang, C. Yan and Q. Zhang, *Angew. Chem., Int. Ed.*, 2017, **129**, 7872–7876.
31 K. Yan, Z. Lu, H.-W. Lee, F. Xiong, P.-C. Hsu, Y. Li, J. Zhao, S. Chu and Y. Cui, *Nat. Energy*, 2016, **1**, 16010.
32 C. Yang, Y. Yao, S. He, H. Xie, E. Hitz and L. Hu, *Adv. Mater.*, 2017, **29**, 1702714.
33 X. L. Li, S. Huang, D. Yan, J. Zhang, D. Fang, Y. V. Lim, Y. Wang, T. C. Li, Y. Li, L. Guo and H. Y. Yang, *Energy Environ. Mater.*, 2022, DOI: **10.1002/eem2.12274**.
34 Y. Fang, S. L. Zhang, Z. P. Wu, D. Luan and X. W. Lou, *Sci. Adv.*, 2021, **7**, eabg3626.
35 G. Li, Z. Liu, Q. Huang, Y. Gao, M. Regula, D. Wang, L.-Q. Chen and D. Wang, *Nat. Energy*, 2018, **3**, 1076–1083.
36 H. Shi, C. J. Zhang, P. Lu, Y. Dong, P. Wen and Z. S. Wu, *ACS Nano*, 2019, **13**, 14308–14318.
37 Q. Song, H. Yan, K. Liu, K. Xie, W. Li, W. Gai, G. Chen, H. Li, C. Shen, Q. Fu, S. Zhang, L. Zhang and B. Wei, *Adv. Energy Mater.*, 2018, **8**, 1800564.
38 K. Bindumadhavan, P. Y. Chang and R. Doong, *Electrochim. Acta*, 2017, **243**, 282–290.
39 T. Liu, S. Chen, W. Sun, L. P. Lv, F. H. Du, H. Liu and Y. Wang, *Adv. Funct. Mater.*, 2021, **31**, 2008514.
40 X. He, Y. Yang, M. S. Cristian, J. Wang, X. Hou, B. Yan, J. Li, T. Zhang, E. Paillard, M. Swietoslawski, R. Kostecki, M. Winter and J. Li, *Nano Energy*, 2020, **67**, 104172.

 